Two-dimensional optomechanical crystal resonator in gallium arsenide

Rhys G. Povey,[1,2] Ming-Han Chou,[1,2] Gustav Andersson,[2] Christopher R. Conner,[2] Joel Grebel,[2] Yash J. Joshi,[2] Jacob M. Miller,[1,2] Hong Qiao,[2] Xuntao Wu,[2] Haoxiong Yan,[2] and Andrew N. Cleland[2,3,*]

[1] *Department of Physics, University of Chicago, Chicago, Illinois 60637, USA*

[2] *Pritzker School of Molecular Engineering, University of Chicago, Chicago, Illinois 60637, USA*

[3] *Center for Molecular Engineering and Materials Science Division, Argonne National Laboratory, Lemont, Illinois 60439, USA*

(Received 27 July 2023; revised 20 November 2023; accepted 14 December 2023; published 10 January 2024)

In the field of quantum computation and communication, there is a compelling need for quantum coherent frequency conversion between microwave electronics and infrared optics. A promising platform for this is an optomechanical crystal resonator that uses simultaneous photonic and phononic crystals to create a colocalized cavity coupling an electromagnetic mode to an acoustic mode, which then via electromechanical interactions can undergo direct transduction to electronics. The majority of the work in this area has been on one-dimensional nanobeam resonators, which provide strong optomechanical couplings but, due to their geometry, suffer from an inability to dissipate heat produced by the laser pumping required for operation. Recently, a quasi-two-dimensional optomechanical crystal cavity has been developed in silicon, exhibiting similarly strong coupling with better thermalization but at a mechanical frequency above optimal qubit operating frequencies. Here, we adapt this design to gallium arsenide, a natural thin-film single-crystal piezoelectric that can incorporate electromechanical interactions, obtaining a mechanical resonant mode at $f_{\mathrm{m}} \approx 4.5$ GHz that is ideal for superconducting qubits and demonstrating optomechanical coupling of $g_{\mathrm{om}}/(2\pi) \approx 650$ kHz.

DOI: 10.1103/PhysRevApplied.21.014015

I. INTRODUCTION

Spurred on by the promise of quantum computing [1,2], superconducting qubits [3–9] have become a ubiquitous topic of research and development. These devices, typically operating with microwave electronic frequencies of 4–8 GHz and housed in dilution refrigerators at approximately 10 mK, are excellent candidates for quantum information processing but suffer from an inability to engage in long-range communication due to the lossy environment and large amount of microwave thermal noise at room temperature. To facilitate such connections outside of cryogenic temperatures, a quantum transducer that is able to coherently convert a microwave-electronic quantum state to an infrared fiber-optic signal, ideally in the telecom band of 1530–1565 nm, is desired [10–13]. Of the many approaches being explored for this challenging task, a propitious route is through an optomechanical crystal cavity [14,15] that emerges by placing a defect in a simultaneous photonic and phononic crystal. This defect site is able to support both a microwave-frequency acoustic resonant mode and an infrared electromagnetic resonant mode, allowing them to couple to each other. Acoustic modes can then be directly transduced to electrical signals through a piezoelectric material.

The optomechanical Hamiltonian for an optical resonant mode at ω_{o}, annihilation operator $\hat{a}$, and a mechanical resonant mode at ω_{m}, annihilation operator $\hat{b}$, is given by

$$\hat{H} = \hbar\omega_{\mathrm{o}}\hat{a}^{\dagger}\hat{a} + \hbar\omega_{\mathrm{m}}\hat{b}^{\dagger}\hat{b} + \hbar g_{\mathrm{om}}\hat{a}^{\dagger}\hat{a}\left(\hat{b}^{\dagger}+\hat{b}\right), \quad (1)$$

where the interaction term, with optomechanical coupling g_{om}, can be derived by considering an optical Fabry-Perot mirror attached to a mechanical spring undergoing small oscillations [16,17]. To obtain an exchange interaction, we need to include a strong laser pump at frequency ω_{L}, adding the term $\hbar L\hat{a}^{\dagger}\ \mathrm{e}^{-\mathrm{i}\omega_{\mathrm{L}}t}$, where L is a measure of the pump strength. For a strong pump, we can expand $\hat{a}(t) = \hat{a}'(t) + \bar{a}\ \mathrm{e}^{-\mathrm{i}\,\omega_{\mathrm{L}}t}$, with $\bar{a} \propto L$, and linearize for $\bar{a} \gg \hat{a}'$. With the laser red detuned from the optical resonance, $\omega_{\mathrm{L}} = \omega_{\mathrm{o}} - \omega_{\mathrm{m}}$, under the rotating-wave approximation our interaction term then becomes

$$\hat{H}_{\mathrm{int}} \approx \hbar\, g_{\mathrm{om}}\left(\bar{a}^{*}\hat{a}'\hat{b}^{\dagger}+\bar{a}\hat{a}'^{\dagger}\hat{b}\right), \quad (2)$$

*anc@uchicago.edu

providing a "beam-splitter" swapping interaction that allows infrared optical excitations to be exchanged with microwave-frequency mechanical excitations. As can be seen in Eq. (2), the optomechanical swapping interaction is enhanced by the average photon number, $|\bar{a}|^2$, which is proportional to the laser pump power. Thus, to maximize the effective optomechanical coupling, the laser pump should be as strong as possible before detrimental effects, such as heating, set in.

Previous work [18–20] and the majority of attention in optomechanical crystals for transduction has been on one-dimensional (1D) nanobeam designs [21–26]. These structures exhibit strong optomechanical coupling, $g_{\mathrm{om}}/(2\pi) \sim 1$ MHz, and high mechanical and optical quality factors but are plagued by poor heat dissipation due to their 1D nature, which limits thermal conductivity [27]. Recently, a quasi-two-dimensional (quasi-2D) optomechanical cavity design consisting of C-shape holes within the waveguide of a snowflake hole crystal lattice has been demonstrated in silicon [28]. This device has shown improved heat management while maintaining good optomechanical coupling and quality factors; however, targeting 194 THz optics, it operates at a mechanical frequency near 10 GHz—somewhat above the optimal frequency for popular superconducting qubit archetypes. Here, we adapt the design to gallium arsenide (GaAs), which has half the acoustic wave speed of silicon, to produce a 2D optomechanical resonator at a superconducting-qubit-compatible frequency of approximately 5 GHz. Furthermore, the inherent piezoelectricity in gallium arsenide allows for future direct coupling to an electrical circuit.

II. DESIGN

To describe the symmetries present in the optomechanical crystal design, we use the notation $\overset{\pm}{x}$ to denote a mirror (+) or antimirror (−) symmetry through the $x = 0$ plane, such that $P_{\overset{\pm}{x}} \cdot F[P_{\overset{\pm}{x}} \cdot \vec{r}] = \pm F[\vec{r}]$ for some tensor field F, where P is the Householder reflection transform. The main 2D optomechanical crystal is made from snowflake-shaped holes in a periodic lattice that exhibits $\pi/3$ rotational symmetry and mirror symmetries (wallpaper group p6m). This provides a complete acoustic band gap and a z mirror-symmetric ($\overset{+}{z}$) electromagnetic band gap [29]. The removal of a row of snowflakes, and additional stretching, creates a waveguide through the 2D optomechanical crystal. C-shape holes along this waveguide in a "vertebrae" pattern form a 1D optomechanical crystal that can be gradually transitioned to create a defect cavity. The layout and parametrization of these holes to form the resonator is presented in Fig. 1(a).

The C-shape-hole dimensions in the gradient region between the mirror and the defect are scaled according to the differentiable $\mathrm{SmoothStep}_1$ function, plotted in

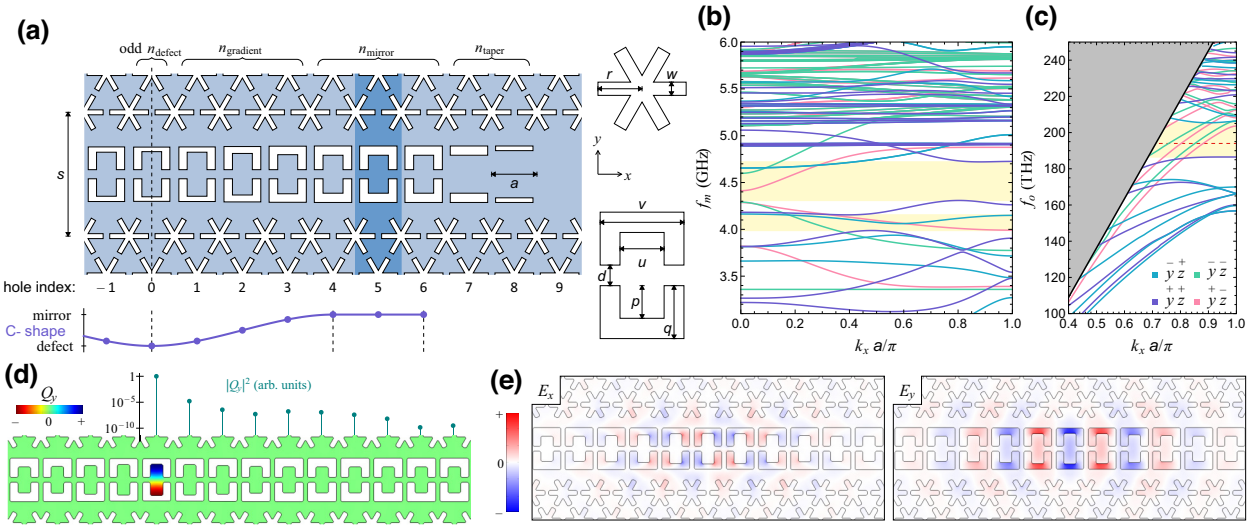

FIG. 1. (a) The layout and geometric parametrization of the optomechanical crystal resonator. The crystal (mirror) unit cell is highlighted. The parameter values in the gradient section between the defect and crystal unit cells are scaled with a $\mathrm{SmoothStep}_1$ function plotted by the purple line below. (b) The acoustic dispersion relations from finite-element-model simulations of the mirror unit cell. Band gaps for $\overset{+}{y}\overset{+}{z}$ symmetric modes are highlighted by yellow bands. (c) The electromagnetic dispersion relations from finite-element-model simulations of the mirror unit cell. Band gaps for $\overset{+}{z}$ symmetric modes are highlighted in yellow and cover our infrared frequency of interest, 194 THz, marked with a dashed red line. (d) Simulation of the displacement field, Q_y, for the paddle breathing mode at 4.63 GHz. Displacements in paddles neighboring the defect are too small to make out but are plotted above on a log scale. (e) Simulations of the electric field for an electromagnetic resonance at 197 THz. The specific dimensions used for the simulations are given in the Supplemental Material [29].

Fig. 1(a), with the definition $\text{SmoothStep}_n : [0,1] \to [0,1]$ by $x \mapsto x^{n+1} \sum_{k=0}^{n} \binom{n+k}{k} \binom{2n+1}{n-k} (-x)^k$, where $\binom{n}{k}$ are binomial coefficients. This is the lowest-order polynomial between constant 0 and 1 that is n differentiable.

Here, we focus on $n_{\text{defect}} = 1$ single-paddle resonances. Although $n_{\text{defect}} > 1$ resonators provide better optomechanical couplings in simulation, they are prone to fabrication imperfections, splitting the resonance into separate modes. The simulations show that a 1 nm increase in paddle length (p) shifts the individual resonance by -17 MHz.

Starting with C-shape hole parameters used in silicon [28,30], finite-element-model simulations [31] have been carried out in gallium arsenide and iterated upon to find a set of dimensions that produce the desired band gaps. The dispersion relations for such parameters over a vertebrae unit cell are given in Figs. 1(b) and 1(c). The acoustic resonance displacement field must be mirror symmetric about every geometric mirror plane in order to have nonvanishing optomechanical coupling [29,32]. For the vertebrae resonator design, this is the paddle breathing mode, with mirror symmetries about each cardinal plane through the center $(^{+}_{x}\,^{+}_{y}\,^{+}_{z})$ as depicted in Fig. 1(d). By changing the paddle length (p) between the mirror cell and the defect cell, we can move the breathing mode from outside the band gap to within.

Eigenvalue simulations of the full vertebrae resonator are shown in Figs. 1(d) and 1(e). In order to accommodate future acoustic piezoelectric wave propagation, the waveguide is aligned along the [110] GaAs crystal axis [32]. With sufficiently large models, the optical-mode quality factor has been simulated to be approximately 26×10^3. Simulations for the mechanics, which only include loss through the supports, yield mechanical quality factors in excess of 10^9. The actual mechanical quality factors will be significantly less than this.

The optomechanical coupling, calculated from displacement and electric fields, has a contribution of 358 kHz from the moving boundary and 241 kHz from the photoelastic effect, giving a total of $g_{\text{om}}/(2\pi) = 599$ kHz.

Simulations of heat dissipation comparing the 2D vertebrae design to a 1D nanobeam are available in the Supplemental Material [29]. While the heating is highly dependent on the size of the structure, the 2D design offers superior scaling. For the same heating power, a vertebrae optomechanical resonator exhibits a temperature increase that is an order of magnitude lower than that for a 40-μm-long nanobeam.

III. FABRICATION

Devices are fabricated on heterostructure wafers consisting of 250 nm of GaAs, on a 1-μm $Al_{0.9}Ga_{0.1}As$ sacrificial layer, on 635-μm bulk (100) GaAs. The relatively low suspension height provided by the sacrificial layer ($t_{\text{gap}} < \lambda_o$) leads to optical fields leaking into the bulk, limiting the optical quality factors and the grating coupler performance. Simulations of the dependence of the optical quality factor on the suspension height are provided in the Supplemental Material [29].

Patterning is performed with electron-beam lithography using 14 wt% hydrogen silsesquioxane in methyl isobutyl ketone resist and etched using an inductively-coupled plasma struck in a chlorine-argon gas mixture. Proximity-effect correction is vital when patterning nanometer-scale features over hundreds of square microns on a heavy substrate with significant electron back scatter (details of the point-spread function used are provided in the Supplemental Material [29]). To account for uncertainty in the precise slab thickness, the hole sizes produced, and the simulations, the devices are fabricated in a series of varying global scale factors, typically in steps of 1%. Parameter dimensions for the pattern used to write the device presented here are listed in the Supplemental Material [29].

To couple light to the device, two suspended-grating coupler pads are used to deflect light in and out of plane to optical fibers positioned above the device. The resonator is then interposed along a connecting suspended waveguide as depicted in Figs. 2(a) and 2(b). Although less efficient than tapered-beam edge coupling, this approach allows up to 100 devices to be fabricated and tested on a single 1-cm^2 chip.

IV. MEASUREMENT

The optical measurements are carried out at room temperature using an infrared fiber-optic setup and a tunable laser. A simplified diagram including only major elements is shown in Fig. 2(c). To compensate for slow thermal drifts of the optical resonance frequency and the overall transmission, a second-harmonic dither-locking system is used to track the resonance inflection points. A diagram of the complete setup, and details on the dither locking, are included in the Supplemental Material [29].

Transmission through the optical resonance is given by

$$|S_{21}(\omega)|^2 = \frac{\left(\gamma_{o,wg}\right)^2}{(\omega - \omega_o)^2 + \left(\frac{\gamma_o}{2}\right)^2},$$

with $\gamma_o = \gamma_{o,0} + 2\gamma_{o,wg}$, where $\gamma_{o,0}$ is the intrinsic power-loss rate and $\gamma_{o,wg}$ is the power-loss rate to each waveguide port. The loaded quality factor is defined as $Q_{o,L} = \omega_o/\gamma_o$ and the internal quality factor is $Q_{o,0} = \omega_o/\gamma_{o,0}$. A captured transmission profile is given in Fig. 3(a).

At room temperature, the mechanical resonance has a thermal population $\bar{n}_m \approx k_B T/\hbar\omega_m = 1371 \pm 14$, which through the optomechanical interaction will modulate the optical resonance at the mechanical resonance frequency. Probing the side of the optical resonance, we monitor the

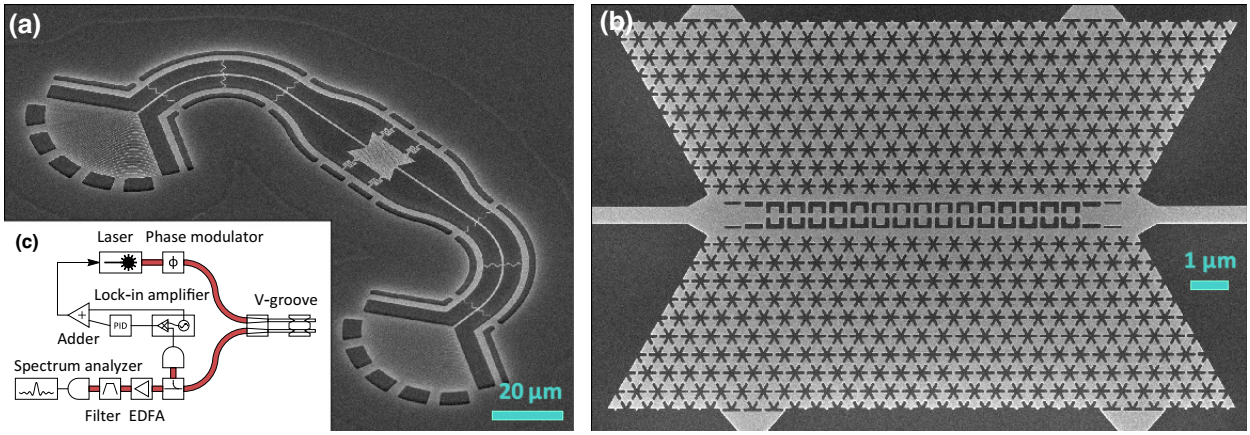

FIG. 2. (a) A scanning-electron-microscope image, taken at 45°, of a device similar to the one measured here. Two large suspended-grating coupler pads deflect light in and out of plane to couple to overhead optical fibers. The optomechanical crystal plate is suspended in the middle with large serpentine tethers to relieve tension during the release process. (b) An enlarged image of the optomechanical plate from (a), taken top down, showing the vertebrae resonator. Proximity-effect correction during electron-beam lithography is essential for uniform snowflakes. (c) A simplified diagram of the optical measurement setup, showing only elements discussed in the text. The phase modulator is driven by a microwave-frequency signal generator and provides a calibration of the power measured by the spectrum analyzer. The V-groove assembly holds the fiber optics above the device. A portion of the output signal is used in a dither-locking system, utilizing a lock-in amplifier and a proportional-integral-derivative (PID) controller, that adjusts the laser's output frequency. The detection chain consists of an erbium-doped fiber amplifier (EDFA) followed by a filter to cut out amplified spontaneous emission and then a microwave-frequency bandwidth photodetector.

resulting power fluctuations using a high-bandwidth photodetector, and using a spectrum analyzer we can observe the mechanical thermal spectrum.

Conveniently, the transmission factor of this optomechanical spectrum is identical to the transmission factor of a weak phase-modulated signal [33], allowing us to make a calibrated measurement of the optomechanical coupling. At laser frequency ω_L, the phase-modulated input is $\exp[-i\,\omega_L t + i\,A_\Phi \sin[\omega_\Phi t]]$. For hot optomechanics, $\bar{n}_m \gg 1$, and weak phase modulation, $A_\Phi \ll 1$, our power spectral density is, to leading order in A_Φ, [29,32]

$$S_{XX}(\omega > 0) \approx \mathcal{T}(\omega_L;\omega)\left(g_{om}{}^2 \frac{\bar{n}_m\gamma_m}{(\omega-\omega_m)^2+\left(\frac{\gamma_m}{2}\right)^2} + \frac{A_\Phi{}^2\omega_\Phi{}^2}{4} 2\pi\delta(\omega-\omega_\Phi)\right), \tag{3}$$

where $\gamma_m = \omega_m/Q_m$ is the mechanical-mode power-loss rate and $\mathcal{T}(\omega_L;\omega)$ is a complicated function of the laser frequency and the spectrum frequency that includes transmission through the optical cavity and all efficiencies. Using a spectrum analyzer with window function $w(f_{SA},f_{RBW};f)$, where f_{SA} is the measurement frequency and f_{RBW} is the resolution bandwidth, with step size $\Delta f_{SA} \ll f_{RBW} \ll \gamma_m/(2\pi)$, the measured power is

$$P(\omega_{SA}) = \mathcal{T}(\omega_L;\omega_{SA})\left(f_{RBW} 2 g_{om}{}^2 \frac{\bar{n}_m\gamma_m}{(\omega_{SA}-\omega_m)^2+\left(\frac{\gamma_m}{2}\right)^2} + \frac{A_\Phi{}^2\omega_\Phi{}^2}{2} w(\omega_{SA},f_{RBW};\omega_\Phi) + \mathrm{bg}\right).$$

A broad background, denoted by bg, can be removed with a low-order polynomial fit. If $\omega_\Phi \approx \omega_m$, then $\mathcal{T}(\omega_L;\omega_{SA})$ is approximately constant. Fitting the window function over the phase-modulated signal (with known amplitude A_Φ) allows us to determine $\mathcal{T}$; then fitting the thermal spectrum gives us g_{om}. For fast scans with no averaging, there is a dither imprint that can be included in the fit or ignored.

In practice, a fit over the thermal spectrum gives us ω_m, γ_m and the parameter $\mathcal{A} = 2\,\mathcal{T}\,g_{om}{}^2\,\bar{n}_m\,\gamma_m$, while a window fit over the phase-modulation signal gives us $P_{f_\Phi} = \mathcal{T}\,A_\Phi{}^2\,\omega_\Phi{}^2/2$, such that

$$g_{om} = \frac{\omega_\Phi A_\Phi}{\sqrt{k_B T/\hbar}}\sqrt{\frac{\omega_m \mathcal{A}}{4\gamma_m P_{f_\Phi}}}. \tag{4}$$

Spectrum scans are fitted individually, with each producing $\sqrt{\omega_m\mathcal{A}/4\gamma_m P_{f_\Phi}}$, and these are combined together to give a factor that contains all the statistical uncertainty. The temperature, T, and the phase-modulation strength, A_Φ, are included with systematic uncertainties.

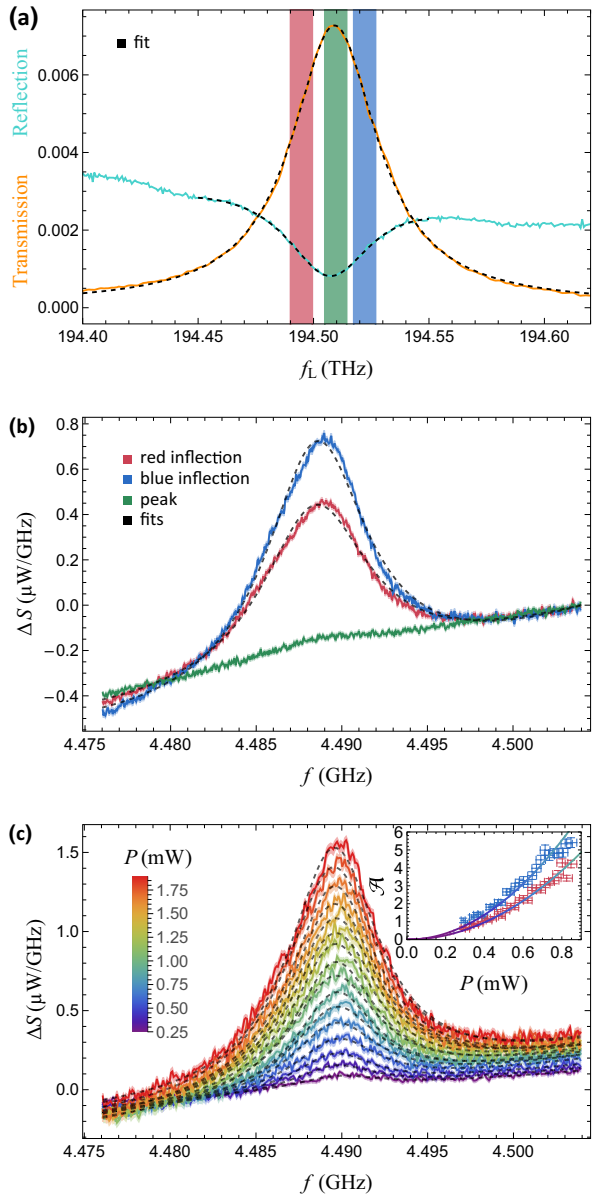

FIG. 3. (a) The full system optical transmission (orange) and reflection (cyan) with color-coded probing regions covered by the dither lock. The transmission includes the waveguide, the grating coupler, the fiber-optic components, and the detector efficiencies. (b) The thermal mechanical spectrum imprinted on the optical signal when probed at the optical resonance and inflection points (color coded accordingly). Each trace is the average of 100 scans with a 100-point moving average and a statistical uncertainty of ± 1 standard deviation is depicted in light shading about the trace. (c) Scans of the thermal mechanical spectrum with different input powers, referenced to the V-groove assembly. The inset shows the fitted spectrum amplitude $\mathcal{A}$ as a function of the input power over the linear operating regime of our photodetector, with P^2 fit curves.

The inset of Fig. 3(a) shows the transmission through, and the reflection from, the optical resonance: Fits give $f_o = 194.5$ THz with loaded quality factor $Q_{o,L} \approx 4300$ and internal quality factor $Q_{o,0} \approx 8600$. Using a first-harmonic dither lock to the resonance peak (shown in green), there is no optomechanical spectrum visible, as expected. With a second-harmonic dither lock to either of the resonance inflection points (blue and red), the thermal optomechanical spectrum can be seen at $f_m = 4.488$ GHz, with quality factor $Q_m \approx 600$. Figure 3(b) shows the optomechanical spectrum averaged over 100 scans.

Optomechanical couplings are calculated for each individual scan by fitting the thermal spectrum and the phase-modulated signal. The weighted mean from 100 scans at both the blue and red inflection points yields $g_{om}/(2\pi) = (649 \pm 8)$ kHz.

Scans made at varying laser probe powers are shown in Fig. 3(c). The current output of our photodetector is proportional to the laser power received, giving the power of the measured signal proportional to the square of laser power. This scaling of the thermal-power-spectrum amplitude, $\mathcal{A}$, is shown in the inset.

V. DISCUSSION AND CONCLUSION

We have demonstrated a quasi-2D optomechanical resonator in gallium arsenide, using the vertebrae design, with an optical resonance in the infrared C band and mechanical resonance at approximately 4.5 GHz, compatible with transmon superconducting qubits. The optomechanical coupling of approximately 650 kHz is slightly less than the best demonstrated couplings of approximately 1 MHz [21,28]; however, there is significant room for improvement in design-parameter optimization, fabrication, and cryogenic operation. Transitioning to edge coupling in reflection will open up the other side of the vertebrae resonator to electromechanical coupling.

The low suspension height of about 1 μm impacts the optical performance, as evidenced by certain devices that were warped out of plane and that demonstrated higher optical quality factors. Unfortunately, this likely has a negative impact on the mechanical performance. The high aluminum content in the sacrificial layer, in addition to hastening the release process, also has a tendency to leave behind difficult-to-remove compounds. Switching to a 3 μm $Al_{0.7}Ga_{0.3}As$ sacrificial layer should provide easily obtainable gains [21]. The corresponding gentler release would further allow removal of the flexible tethers supporting the optomechanical crystal to realize more thermal contact to the larger chip.

Pattern-fabrication precision for 2D devices is challenging compared to 1D devices, particularly with the high atomic weight substrate, which exhibits strong electron-beam proximity effects. Minor imperfections in the optomechanical crystal are inherently more common and degrade both the optical and the mechanical quality factors.

ACKNOWLEDGMENTS

We would like to thank Peter Duda for helpful discussions. This work was supported by the Laboratory for Physical Sciences (LPS)–U.S. Army Research Office (ARO) Award No. W911NF-23-1-0077, the National Science Foundation (NSF) Quantum Leap Challenge Institute (QLCI) for Hybrid Quantum Architectures and Networks (HQAN) (Award No. 2016136), by the Air Force Office of Scientific Research, and in part based on work supported by the U.S. Department of Energy Office of Science National Quantum Information Science Research Centers, and by the University of Chicago Materials Research Science and Engineering Center (MRSEC) (NSF Award No. DMR-2011854). This work made use of the Pritzker Nanofabrication Facility, part of the Pritzker School of Molecular Engineering at the University of Chicago, which receives support from Soft and Hybrid Nanotechnology Experimental (SHyNE) Resource (NSF ECCS-2025633), a node of the NSF National Nanotechnology Coordinated Infrastructure.

[1] A. Steane, Quantum computing, Rep. Progr. Phys. **61**, 117 (1998).
[2] J. Preskill, Quantum computing in the NISQ era and beyond, Quantum **2**, 79 (2018).
[3] Y. Nakamura, Y. A. Pashkin, and J. S. Tsai, Coherent control of macroscopic quantum states in a single-Cooper-pair box, Nature **398**, 786 (1999).
[4] J. Q. You and F. Nori, Quantum information processing with superconducting qubits in a microwave field, Phys. Rev. B **68**, 064509 (2003).
[5] A. Blais, R.-S. Huang, A. Wallraff, S. M. Girvin, and R. J. Schoelkopf, Cavity quantum electrodynamics for superconducting electrical circuits: An architecture for quantum computation, Phys. Rev. A **69**, 062320 (2004).
[6] L. Frunzio, A. Wallraff, D. Schuster, J. Majer, and R. Schoelkopf, Fabrication and characterization of superconducting circuit QED devices for quantum computation, IEEE Trans. Appl. Supercond. **15**, 860 (2005).
[7] G. Wendin, Quantum information processing with superconducting circuits: A review, Rep. Progr. Phys. **80**, 106001 (2017).
[8] S. Kwon, A. Tomonaga, G. L. Bhai, S. J. Devitt, and J.-S. Tsai, Gate-based superconducting quantum computing, J. Appl. Phys. **129**, 041102 (2021).
[9] Y. Y. Gao, M. A. Rol, S. Touzard, and C. Wang, Practical guide for building superconducting quantum devices, PRX Quantum **2**, 040202 (2021).
[10] N. J. Lambert, A. Rueda, F. Sedlmeir, and H. G. L. Schwefel, Coherent conversion between microwave and optical photons: An overview of physical implementations, Adv. Quantum Technol. **3**, 1900077 (2020).
[11] N. Lauk, N. Sinclair, S. Barzanjeh, J. P. Covey, M. Saffman, M. Spiropulu, and C. Simon, Perspectives on quantum transduction, Quantum Sci. Technol. **5**, 020501 (2020).
[12] Y. Chu and S. Gröblacher, A perspective on hybrid quantum opto- and electromechanical systems, Appl. Phys. Lett. **117**, 150503 (2020).
[13] G. Moody, *et al.*, 2022 roadmap on integrated quantum photonics, J. Phys.: Photonics **4**, 012501 (2022).
[14] M. Eichenfield, J. Chan, R. M. Camacho, K. J. Vahala, and O. Painter, Optomechanical crystals, Nature **462**, 78 (2009).
[15] A. H. Safavi-Naeini and O. Painter, Design of optomechanical cavities and waveguides on a simultaneous bandgap phononic-photonic crystal slab, Opt. Express **18**, 14926 (2010).
[16] M. Aspelmeyer, T. J. Kippenberg, and F. Marquardt, Cavity optomechanics, Rev. Mod. Phys. **86**, 1391 (2014).
[17] M. Aspelmeyer, T. J. Kippenberg, and F. Marquardt, eds., *Cavity Optomechanics*, Quantum Science and Technology (Springer-Verlag Berlin, Heidelberg, 2014).
[18] J. Bochmann, A. Vainsencher, D. D. Awschalom, and A. N. Cleland, Nanomechanical coupling between microwave and optical photons, Nat. Phys. **9**, 712 (2013).
[19] A. Vainsencher, K. J. Satzinger, G. A. Peairs, and A. N. Cleland, Bi-directional conversion between microwave and optical frequencies in a piezoelectric optomechanical device, Appl. Phys. Lett. **109**, 033107 (2016).
[20] G. A. Peairs, M.-H. Chou, A. Bienfait, H.-S. Chang, C. R. Conner, É. Dumur, J. Grebel, R. G. Povey, E. Şahin, K. J. Satzinger, Y. P. Zhong, and A. N. Cleland, Continuous and time-domain coherent signal conversion between optical and microwave frequencies, Phys. Rev. Appl. **14**, 061001(R) (2020).
[21] M. Forsch, R. Stockill, A. Wallucks, I. Marinković, C. Gärtner, R. A. Norte, F. van Otten, A. Fiore, K. Srinivasan, and S. Gröblacher, Microwave-to-optics conversion using a mechanical oscillator in its quantum ground state, Nat. Phys. **16**, 69 (2019).
[22] M. Mirhosseini, A. Sipahigil, M. Kalaee, and O. Painter, Superconducting qubit to optical photon transduction, Nature **588**, 599 (2020).
[23] W. Jiang, C. J. Sarabalis, Y. D. Dahmani, R. N. Patel, F. M. Mayor, T. P. McKenna, R. V. Laer, and A. H. Safavi-Naeini, Efficient bidirectional piezo-optomechanical transduction between microwave and optical frequency, Nat. Commun. **11**, 1166 (2020).
[24] G. Arnold, M. Wulf, S. Barzanjeh, E. S. Redchenko, A. Rueda, W. J. Hease, F. Hassani, and J. M. Fink, Converting microwave and telecom photons with a silicon photonic nanomechanical interface, Nat. Commun. **11**, 4460 (2020).
[25] R. Stockill, M. Forsch, F. Hijazi, G. Beaudoin, K. Pantzas, I. Sagnes, R. Braive, and S. Gröblacher, Ultra-low-noise microwave to optics conversion in gallium phosphide, Nat. Commun. **13**, 6583 (2022).
[26] S. Hönl, Y. Popoff, D. Caimi, A. Beccari, T. J. Kippenberg, and P. Seidler, Microwave-to-optical conversion with a gallium phosphide photonic crystal cavity, Nat. Commun. **13**, 2065 (2022).
[27] G. S. MacCabe, H. Ren, J. Luo, J. D. Cohen, H. Zhou, A. Sipahigil, M. Mirhosseini, and O. Painter, Nano-acoustic resonator with ultralong phonon lifetime, Science **370**, 840 (2020).
[28] H. Ren, M. H. Matheny, G. S. MacCabe, J. Luo, H. Pfeifer, M. Mirhosseini, and O. Painter, Two-dimensional

optomechanical crystal cavity with high quantum cooperativity, Nat. Commun. **11**, 3373 (2020).

[29] See the Supplemental Material at http://link.aps.org/supplemental/10.1103/PhysRevApplied.21.014015 which provides additional discussion and measurements.

[30] C. M. Kersul, R. Benevides, F. Moraes, G. H. M. de Aguiar, A. Wallucks, S. Gröblacher, G. S. Wiederhecker, and T. P. M. Alegre, Silicon anisotropy in a bi-dimensional optomechanical cavity, APL Photonics **8**, 056112 (2023).

[31] COMSOL AB, http://www.comsol.com COMSOL MULTIPHYSICS®.

[32] R. G. Povey, Ph.D. thesis, Department of Physics, University of Chicago, Chicago IL (2023), https://knowledge.uchicago.edu/record/7543.

[33] M. L. Gorodetsky, A. Schliesser, G. Anetsberger, S. Deleglise, and T. J. Kippenberg, Determination of the vacuum optomechanical coupling rate using frequency noise calibration, Opt. Express **18**, 23236 (2010).